



**HAL**  
open science

## Analysis of seismic signals recorded on a prone-to-fall rock column (Vercors massif, French Alps)

Clara Lévy, Denis Jongmans, Laurent Baillet

► **To cite this version:**

Clara Lévy, Denis Jongmans, Laurent Baillet. Analysis of seismic signals recorded on a prone-to-fall rock column (Vercors massif, French Alps). *Geophysical Journal International*, 2011, 186 (1), pp.296-310. 10.1111/j.1365-246X.2011.05046.x . hal-00650311

**HAL Id: hal-00650311**

**<https://hal.science/hal-00650311v1>**

Submitted on 26 Mar 2021

**HAL** is a multi-disciplinary open access archive for the deposit and dissemination of scientific research documents, whether they are published or not. The documents may come from teaching and research institutions in France or abroad, or from public or private research centers.

L'archive ouverte pluridisciplinaire **HAL**, est destinée au dépôt et à la diffusion de documents scientifiques de niveau recherche, publiés ou non, émanant des établissements d'enseignement et de recherche français ou étrangers, des laboratoires publics ou privés.

# Analysis of seismic signals recorded on a prone-to-fall rock column (Vercors massif, French Alps)

Clara Levy, Denis Jongmans and Laurent Baillet

ISTerre, CNRS, Grenoble University, BP 53, 38041 Grenoble Cedex 9, France. E-mail: laurent.baillet@ujf-grenoble.fr

Accepted 2011 April 14. Received 2011 April 12; in original form 2010 November 29

## SUMMARY

A small-aperture (40 m) short-period seismic array was installed during four months on the Vercors massif (Western French Alps) at the top of a limestone column which collapsed one month and a half later. During this monitoring period, 193 seismic events were recorded by the seven seismometers of the array. Signal analysis yielded three main types of nearby seismic events to be identified from temporal and spectral characteristics: microearthquakes (single or multiple events), individual block falls and rock falls. It turned out that 60 per cent of the 193 events were classified as microearthquakes, exhibiting distinct *P* and *S* waves, while 17 per cent of these events remained unclassified. Out of the microearthquakes, 40 events with a good signal-to-noise ratio were selected and processed. *P*- and *S*-wave traveltimes were picked on the records and the inferred hypocentral distances agree with the two zones of the scarp exhibiting fresh ruptures after the fall. Polarization analysis of the 3-C records, along with numerical simulations, allowed discriminating between the two possible rupture mechanisms (toppling and sliding). Shear rupture (sliding) was the predominant mode in the lower part of the column whereas traction rupture (toppling) affected the upper part. Finally, the comparison between the ground motions recorded on the column and on the rock mass showed a systematic amplification on the column. Signal processing and numerical modelling both suggest that this amplification resulted from the excitation of the natural frequencies of the column and is particularly high ( $>3$ ) for microearthquakes occurring at the column-to-mass interface.

**Key words:** Fourier analysis; Numerical approximations and analysis; Spatial analysis; Geomechanics; Guided waves; Site effects.

## 1 INTRODUCTION

Small aperture seismic arrays, with a size from a few tens of metres to 1 km, have been increasingly deployed on unstable slopes in the last 10 yr. As gravitational movements affect all types of soils and rocks with a large variety of mechanisms and a wide range of displacement rates (Cruden & Varnes 1996), the objectives of such seismic investigation or monitoring can be manifold. Recording seismic events and/or ambient vibrations with seismic arrays have been used to understand the seismic response of rock slopes (Del Gaudio & Wasowski 2007; Del Gaudio *et al.* 2008; Burjánek *et al.* 2010; Levy *et al.* 2010), to detect and characterize the seismic activity generated by slope deformation in rocks (Mertl & Brückl 2007; Spillmann *et al.* 2007) or in weaker sedimentary material (Walter & Joswig 2008, 2009). Seismic arrays have also been used to study the seismic precursory patterns before a cliff failure (Amitrano *et al.* 2005; Senfaute *et al.* 2009), as well as for detecting small size rock falls (Vilajosana *et al.* 2008; Lacroix & Helmstetter 2010). Another application of such arrays is the achievement of 3-D seismic tomography of landslides (Renalier *et al.* 2010).

A large amount of these studies was devoted to rocky slopes, with the aim of detecting and locating microearthquakes generated by fracturing within the unstable rock mass. During such monitoring experiments, the number of detected seismic events, which depends on the site characteristics and the triggering parameters, is usually very large. During a microseismic investigation on the site of Randa (Swiss Alps), Spillmann *et al.* (2007) operated a 31-month monitoring system that recorded a total of 66 409 triggered events. A major effort was required to classify this data set, from which only 223 landslide-related microearthquakes with magnitudes ranging from  $-2$  to  $0$  were extracted. Other events were identified as noise transients generated by electrical disturbances, distant earthquakes or explosions and regional earthquakes. In a similar study performed on the Sechilienne rock slope (French Alps), Helmstetter & Garambois (2010) detected several thousand events in 2 yr. After rejection of events classified as noise (helicopter, industrial noise and storms), they evidenced mostly block falls, and also hundreds of microearthquakes and local earthquakes. During temporary surveys conducted at the Heumoes (Austrian Alps) and Super-Sauze (French Alps) landslides affecting weak formations (glacial

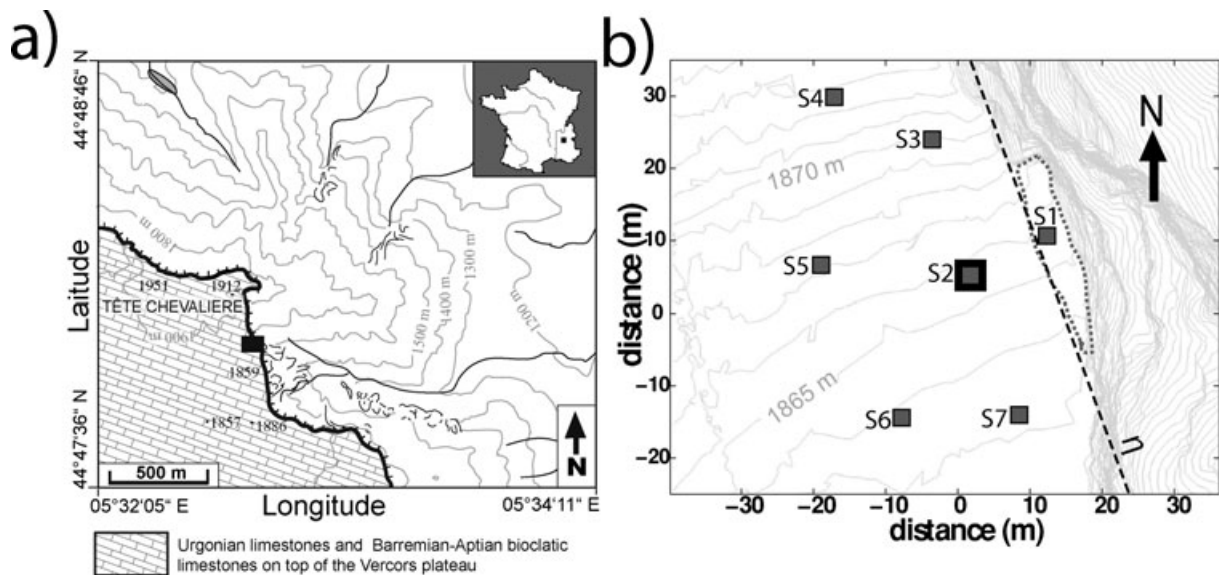


**Figure 1.** (a) Situation map of the Chamousset site located at the border of the Vercors plateau (southeast of France). The cliff limit is delineated with a barbed line and the site is located with a black rectangle. (b) Layout of the seismic array deployed from the 2007 July 2007 to the 2007 October 10. The seven short period seismometers are labelled S1–S7. Vertical seismometers were installed, except for the 3-C seismometer S2. The unstable column is contoured with a grey dashed line. The mean rupture plane  $\eta$  is a black dotted line.

sediments and marls, respectively), Walter & Joswig (2008, 2009) evidenced seismic signals generated by mass movements. At the Super-Sauze mudflow, they distinguished three main types of seismic events from the spectral and temporal signal characteristics: rockfall events, fracture events and scratch events. These examples show that the recorded seismic signals are usually numerous and could be of different origins. Thus, event classification appeared to be a sensitive and time-consuming task, requiring the designing of semi-automatic pattern recognition procedures (Spillmann *et al.* 2007; Helmstetter & Garambois 2010). In a few studies, the seismic events related to the rock slope deformation were tentatively located, using different seismic array techniques (Spillmann *et al.* 2007; Walter & Joswig 2009; Helmstetter & Garambois 2010). Event location however turned out to be a challenging task because of the strong heterogeneity in seismic velocity characterizing the unstable slopes, the high seismic attenuation, and the difficulty to pick identified impulsive waves (first break  $P$  and  $S$  waves) (Spillmann *et al.* 2007). The difficulty of picking impulsive waves is emphasized by the composite or multiple-event character of many events classified as microearthquakes generated by rock slope deformation (Mertl & Brückl 2007). Consequently, a large part of the studies were focused on the search of seismic precursors before slope failure (Amitrano *et al.* 2005; Senfaute *et al.* 2009; Levy *et al.* 2010) and on the relation between seismic events (ruptures, rock falls), displacement rate measurements and climatic parameters (Amitrano *et al.* 2010; Levy *et al.* 2010; Helmstetter & Garambois 2010).

Here we present the results of a 4-month seismic array monitoring conducted on the Chamousset site located at the top of a 300 m high limestone cliff (French Alps). These calcareous cliffs are regularly affected by rock falls (Frayssines & Hantz 2006) with little or no precursors, highlighting the brittle behaviour of the rock mass. The variation of the first resonance frequency of the Chamousset limestone column was studied from seismic noise measurements in a previous work (Levy *et al.* 2010). The evolution of the resonance frequency appeared to be strongly controlled by the temperature. During freeze-thaw cycles a significant drop in resonance frequency was interpreted as the result of rock bridge breakage. This paper

focuses on the seismic events recorded during the same experiment. Several thousands were detected at the Chamousset site, out of which 193 were recorded by all the seven seismometers of the 40 m aperture array. Different types of seismic events were identified and analysed. Contrary to previous experiments, some of these events exhibit clear  $P$  and  $S$  waves, making possible an analysis of the rupture mechanism and an estimation of the hypocentral distance. However, the event location was difficult because of the small array aperture and the heterogeneous velocity field.

## 2 CHAMOUSSET SITE

The Chamousset site is located to the South of the carbonate Vercors massif (western Alps, France), at an elevation of about 1900 m, close to the peak of Tête Chevalière (Fig. 1a).

Seven short period (2 Hz) seismometers were deployed from the 2007 July 13 to the 2007 October 10. The array, with an aperture of about 40 m, included one three-component and six vertical sensors (labelled S1–S7 in Fig. 1b), one of which (S1) being installed on the unstable column. All seismometers were connected to the same acquisition system and signals were sampled at a rate of 1000 Hz. A standard trigger algorithm, based on the ratio of short-time averages STA and long-time averages LTA, was used for detecting seismic events. During acquisition, we applied a low ratio STA/LTA of 6 for extracting events, setting the lengths of the STA and LTA windows to 500 ms and 20 s, respectively. Several thousands of seismic event were recorded during the 4-month period, a large part of which being only detected on one or a few sensors. During processing, a second extraction phase was applied to separate the more energetic events. Events recorded by all sensors with a STA/LTA ratio over 8 were selected. 220 events met this double criterion, among which 27 exhibit features (increasing then decreasing amplitudes through the array) distinctive of human (hikers) and animal activity.

The rock column collapsed on the 2007 November 24 and its volume was estimated to 21 000 m<sup>3</sup> from two lidar scans of the cliff acquired before and after the rockfall (Levy *et al.* 2010).

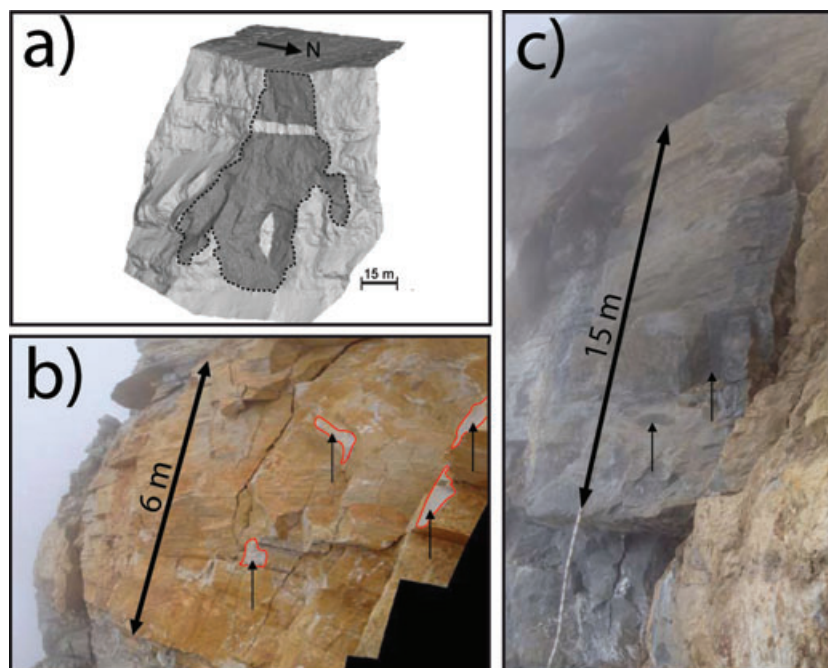


**Figure 2.** (a) Digital Elevation Model of the Chamousset cliff achieved with helicopter lidar data acquired after the column collapse. The rupture plane is in dark grey and the two zones with broken rock bridges are in white. (b) Photo of the 6 m high upper zone showing fresh intact rock rupture (white patches). (c) Photo of the 15 m high lower zone showing fresh intact rock rupture. Some spots showing fresh intact rock rupture are pointed with arrows on (b) and (c). The extent of these rupture surfaces are circled with red on (b).

Unfortunately, the seismic array had to be dismantled on the 2007 October 10 for logistical reasons. After the fall, the rupture plane was inspected by a geologist abseiling the cliff face. He located two zones exhibiting fresh rock rupture surfaces (Fig. 2a): an elongated horizontal zone corresponding to a 6-m-thick limestone bed located 30 m below the plateau, and an elongated vertical 15 m high polyhedron area located 75–90 m below the plateau. Figs 2(a) and (c) show the pictures of these two zones with the broken rock bridges appearing as white patches of 1 dm to a few dm in size.

Two short 30 m long refraction tests were carried out on the plateau, parallel and perpendicular to the cliff. Processing of refracted events and inversion of surface waves gave the following 1-D simplified model (Levy *et al.* 2010): a superficial loose and thin layer ( $V_p = 430 \text{ m s}^{-1}$ ;  $V_s = 185 \text{ m s}^{-1}$ ; 2 m thick) overlying the fractured limestone bedrock ( $V_p = 2800 \text{ m s}^{-1}$ ;  $V_s = 960 \text{ m s}^{-1}$ ).

### 3 SEISMIC SIGNAL CLASSIFICATION

The 193 events recorded by the seven sensors of the array, with a STA/LTA over eight, were analysed and classified (Table 1). As

**Table 1.** Number of events per class type for events detected by all the seven seismometers of the Chamousset site.

Event type	Number
Microearthquake	28
Block fall	8
Rock fall	23
Earthquake or quarry blast	10
Multiple events (Microearthquakes or Block falls or a combination of both)	91
Unclassified	33

stated in the introduction, classification is a difficult task and we started by identifying single events and by characterizing them in the time and frequency domains. The considered parameters are the frequency range, the amplitude, the signal shape and the duration. The event beginning was manually picked and the event end is reached when the mean amplitude of a 0.5 s moving window falls below the noise level preceding the event. Fig. 3 shows the seismograms and spectrograms for four seismic events, recorded on the vertical component of sensor S2. The first one is an artificially generated block fall of a few  $\text{dm}^3$  in size, which is not included in the 193 events. Fig. 3(a) shows that the recorded signal is short and impulsive. The striking feature is the narrow frequency range of the spectrum (around 40 Hz), which is probably related to the size of the block. No specific waves could have been identified at the beginning of the signal. A high number of such mono-frequency impulsive events were found in the data set, with the frequency ranging from 10 to 80 Hz and durations between 0.7 and 2.6 s. One of these events, with a predominant frequency around 60 Hz, is shown in Fig. 3(b).

Another type of impulsive and short duration events is shown in Fig. 3(c). The spectrogram exhibits a broad spectrum (10–100 Hz) with energy bursts at specific frequencies. In the zoomed signal (Fig. 3c, right-hand column), two waves can be clearly distinguished, which were identified as *P* and *S* waves (see the polarization analysis, Section 5, and Fig. 6). The signal envelope has a triangle shape with a coda. 28 events of this type were recorded, with frequencies ranging from 5 to 150 Hz and the duration varying between 0.7 and 3.5 s. These events generating *P* and *S* waves are interpreted as microearthquakes related to the deformation. Their location and mechanism will be studied in Section 5. During the seismic monitoring, we also recorded 10 earthquakes or quarry blasts. Only one of these events, characterized by well separated impulsive *P* and *S* wave onsets (Fig. 3d), was detected by the French permanent

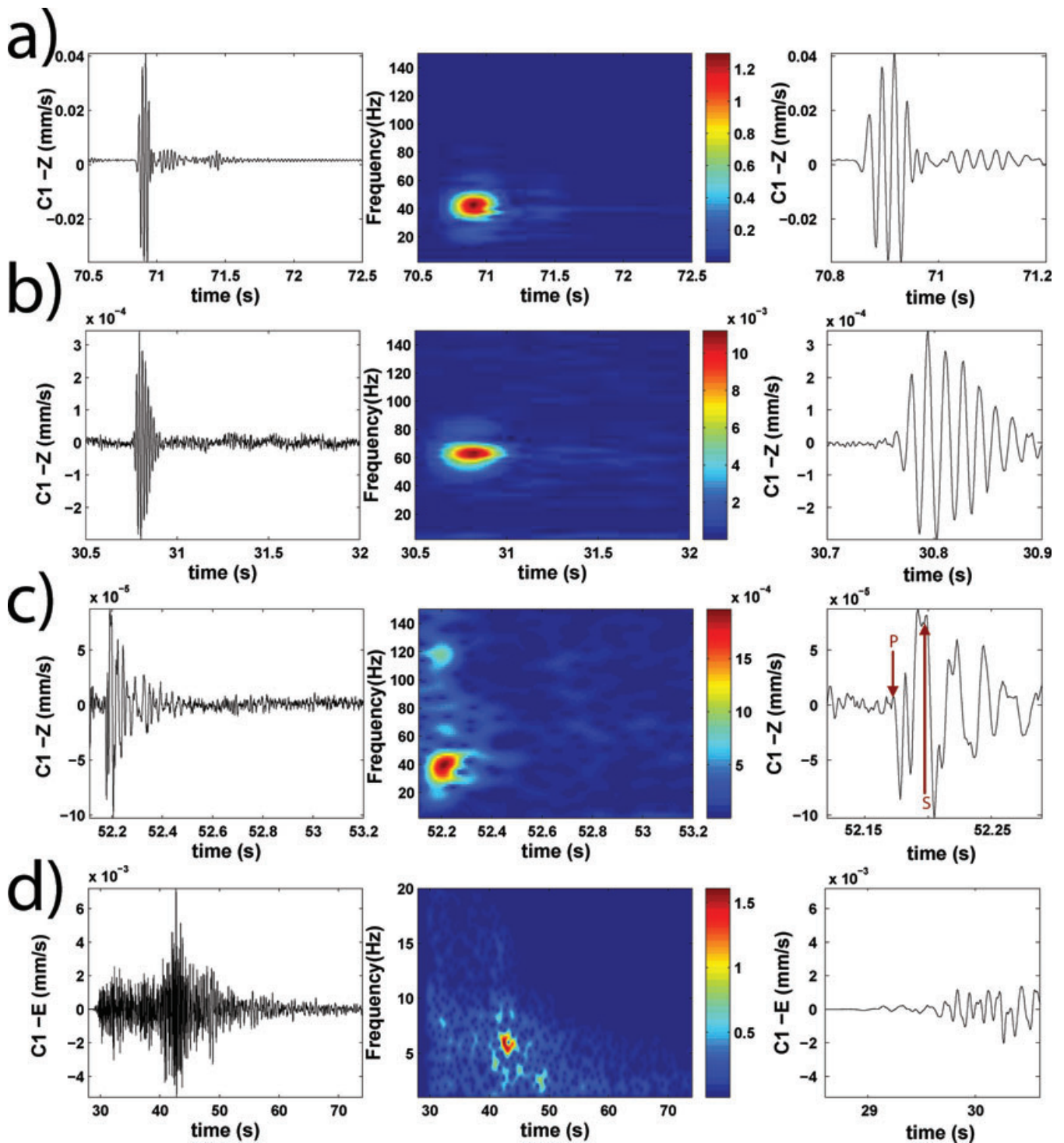


**Figure 3.** Single event seismograms and spectrograms recorded by sensor S2 (located on the rock mass): Left-hand column: full seismogram. Middle column: spectrogram (window length of 0.5 s for a to c and 2s for d with 98 per cent of overlap). Right-hand column: Zoom on the beginning of the signal. (a) Generated block fall - vertical component, recorded on the 2008 July 16 at 09:43:02. (b) Natural block fall - vertical component, recorded on the 2007 July 27 at 11:37:35. (c) Microearthquake - vertical component, recorded on the 2007 September 28 at 15:17:39. *P* and *S* waves arrivals are pointed with red arrows on the zoom window. (d) Earthquake ( $M_L = 3.4$ ; epicentral distance: 112 km)—Horizontal component, recorded on the 2007 October 5 at 06:05:21. Note that the frequency scale is different.

seismological network (SISMALP, Thouvenot *et al.* 1990), indicating that most of these events are local low-magnitude earthquakes and blasts. Their frequency range is notably lower than for the nearby events.

The majority of the recorded events (147 of 193) exhibit complex shapes and were classified into three groups: multiple events, rock falls and unclassified events. Multiple events are made of the succession of separated signals generated by microearthquakes and/or

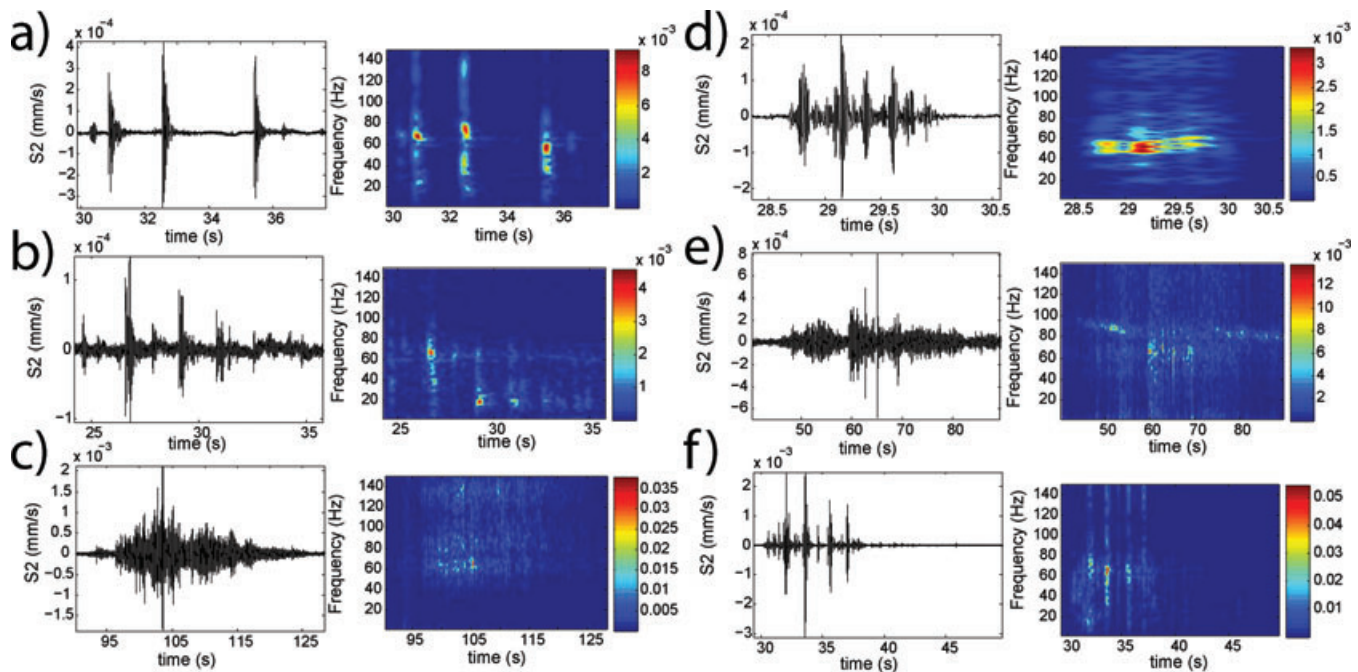


**Figure 4.** Vertical seismograms and spectrograms of composite events recorded by sensor S2 located on the rock mass. Left-hand column: seismogram. Right-hand column: spectrogram (window length of 0.4 s with 98 per cent of overlap). (a) Multiple event with successive microearthquakes, recorded on the 2007 July 25 at 03:12:27. (b) Multiple event with rupture and block fall events, recorded on the 2007 August 17 at 06:00:40. (c) and (d) Rock fall records (2007 August 6 at 09:28:45 and the 2007 July 18 at 13:58:15, respectively). (e) and (f) Unclassified events recorded on the 2007 August 2 at 12:51:04 and the 2007 August 8 at 04:41:54, respectively.

block falls. Signals are considered to be separated when interevent durations of at least 0.5 s with average absolute amplitude below 10 per cent of the event maximum amplitude can be identified. Two examples are shown in Figs 4(a) and (b). In the first case, the record evidences a succession of three main impulsive events (and two minor ones) which were clearly identified as microearthquakes (presence of *P* and *S* waves, triangular envelop shape, broad frequency spectrum with energy bursts). Most of the multiple events exhibit these characteristics. The second record (Fig. 4b), which is characterized by a lower signal-to-noise ratio, also exhibits several impulsive events, which are however more difficult to classify. Spectral characteristics suggest the presence of both microearthquakes and block falls in the signal. During the field campaign, we also recorded 23 signals exhibiting a lemon-shape envelope with spikes and a broad frequency range sometimes spanning the 10–150 Hz range. The signal duration varied between 1.6 and 43 s. Two examples with different frequency ranges and durations are shown in Figs 4(c) and (d). Walter & Joswig (2009) and Helmstetter & Garambois (2010) also detected that type of events that they interpreted as rock falls. Rock falls, with a size varying between a few  $\text{dm}^3$  to a few tens of  $\text{m}^3$  in this case, are complex phenomena with several phases (breakage, detachment, impact, rolling and/or sliding) likely to emit seismic waves with different characteristics (Deparis *et al.* 2008). They often occur with successive detachments, generating complex signals. Other processes, like fragmentation and soil entrainment, could also affect the signal characteristics, in particular the duration. It results that the recorded signals are composite (mixing of emerging phases and spikes) with a broad spectrum that can also be altered by the wave attenuation depending on the distance from the station. Finally, we incorporated all the nearby events with unclear attributes (33) in a class of undetermined events. These could be made up of a complex mixing of nearby rupture events and rock

or block falls with short delays, which made impossible any clear identification. Two such events are shown in Figs 4(e) and (f).

#### 4 CORRELATION WITH METEOROLOGICAL PARAMETERS

The temporal distribution of the 183 seismic events recorded during the 4-month experiment (e.g. without the distant earthquakes and anthropogenic events) is plotted in Fig. 5(a), with two data gaps of 4 and 12 d when the acquisition system was not operating. We grouped the block fall and rock fall events in the same category. The air temperature and the rain fall data measured at a meteorological station located 3.2 km southwestward from the Chamousset site are also plotted in figure (Fig. 5b). Considering that the multiple events are mainly a succession of microearthquakes, the rupture events are predominant with regards to the rock falls. Five peaks appear on the histogram of the number of events, on 2007 August 1, August 8, August 14, August 21 and September 28. Increases in the daily event number are correlated with minima in the temperature curve, which are reached after a significant temperature drop of 15–20 °C. The largest daily number of events was observed when the temperature fell below 0 °C, as Got *et al.* (2010) observed on other seismic data acquired at the same experimental site. On the contrary, no relation emerges between the event number and the rainfall data. These results suggest that temperature drops, which generate thermal contraction stresses, increase the number of microearthquakes resulting from rock breakage. They are in agreement with the analysis of the resonance frequencies on the same site, which also showed a strong temperature control on rock damaging (Levy *et al.* 2010). The correlation between microseismic event clusters and temperature falls was already shown at the foot of the Matterhorn mount (3829 m a.s.l., Italian Alps) in stiff gneissic rocks (Amitrano *et al.* 2010).

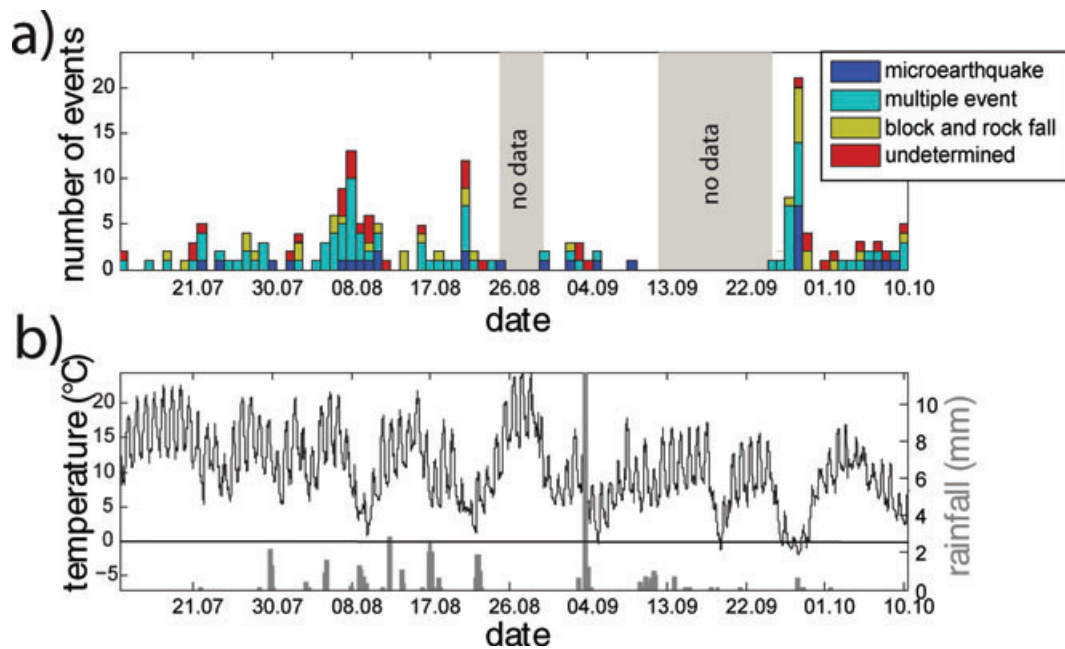


**Figure 5.** (a) Temporal distribution of the 183 events detected on all the seismic array sensors at Chamousset (anthropogenic events were removed from statistics, as well as earthquakes). Events were classified in microearthquakes, multiple events, rock falls (including block falls) and unclassified nearby events, (see text for details). (b) Air temperature curve and rainfall bar diagram recorded at a meteorological station located 3.2 km to the South West from the site and 120 m below in altitude.

On the contrary, the little influence of rainfalls, at least during the experimental period, can be explained by the high permeability in this karstic limestone.

## 5 MICROEARTHQUAKE CHARACTERIZATION

As evidenced in Section 4, most of the recorded seismic events are microearthquakes or a succession of microearthquakes, probably related to the deformation of the prone-to-fall column. Signals classified as microearthquakes systematically exhibit two distinct wave arrivals (Fig. 3a). We performed polarization analysis on the seismograms recorded by the 3-C seismometer S2 in order to identify these waves. Fig. 6 shows the seismograms and the corresponding particle motions for one microearthquake. The polarization analysis was performed on short time windows (15 and 80 ms for the first and second identified waves, respectively). The first arrival (Fig. 6d) exhibits the characteristics of a *P* wave, vibrating along a single, near-vertical direction. This result is consistent with the presence of rupture sources below the sensor. The latter wave is clearly a *S* wave with a near-horizontal polarization (Fig. 6e), perpendicular to the propagation direction given by the *P*-wave vibration. In the horizontal plane, this *S*-wave vibrates along a N80°E direction, almost perpendicular to the orientation of the rupture plane  $\eta$ .

Analysing the wave polarization, we determined *P*- and *S*-wave arrival times for the 40 signals (28 events in the microearthquake class and 12 in the multiple-event class) allowing an accurate picking. The delay times between *P* and *S*-wave arrivals ( $T_s - T_p$ ) were computed for all events and are plotted against time in Fig. 7. Values are ranging from 0.01 to 0.1 s, indicating that microearthquakes are local.  $T_s - T_p$  values were converted into hypocentral distances (Fig. 7), using the seismic model derived from seismic prospecting (see Section 2). The distance uncertainty resulting from picking and velocity uncertainty has been estimated to about 6 m. Most of

the hypocentral distances (except for one higher value) range from 10 to 90 m, and could be consistent with microearthquakes occurring along the interface between the 90 m high column and the rock mass. The two zones where fresh ruptures were observed are shaded in Fig. 7. Considering the depth uncertainty, they concentrate 33 of the 40 microearthquakes.

From the  $T_s - T_p$  values determined at sensor S2 and the *P*-wave arrival times at the other vertical sensors of the seismic network, we attempted to localize the event hypocentres, using the Hypoline software (Joswig 2008). For most events, it was however impossible to find an appropriate hypocentre to explain the data. This failure probably results from the small array aperture (40 m) with regards to the event depth, and from insufficient knowledge on the 3-D seismic structure of the site. Indeed, rock velocities in unstable slope could be extremely heterogeneous (Heincke *et al.* 2006). Spillmann *et al.* (2007) showed that these large velocity variations had to be included in the microearthquake location process. The simple refraction tests made here were unable to produce a 3-D velocity model of the field site.

Magnitudes for the 40 microearthquakes were computed using the estimated hypocentral distances and the displacement amplitudes. The event magnitudes  $M_L$  were derived using the empirical law used by Joswig (2008) for seismic events with a hypocentral distance lower than 3 km

$$M_L = \log_{10}(A_{\max} \times 2800) + [0.25 + \log_{10}(D)], \quad (1)$$

where  $A_{\max}$  is the maximum displacement (in metre) and  $D$  is the hypocentral distance (in km).

Fig. 8(a) shows the magnitude distribution for the 40 events. Microearthquake magnitude ranges from  $-4.5$  to  $-2$ , with most of the events between  $-4$  and  $-2.75$ . Extrapolating empirical relations established for earthquakes (Wells & Coppersmith 1994), the magnitude range ( $-4$ ,  $-3$ ) corresponds to a rupture area between 0.01 and 0.1 m<sup>2</sup>, which matched the size of the observed individual fresh rupture surfaces (Figs 2b and c). Gibowicz *et al.* (1991) analysed

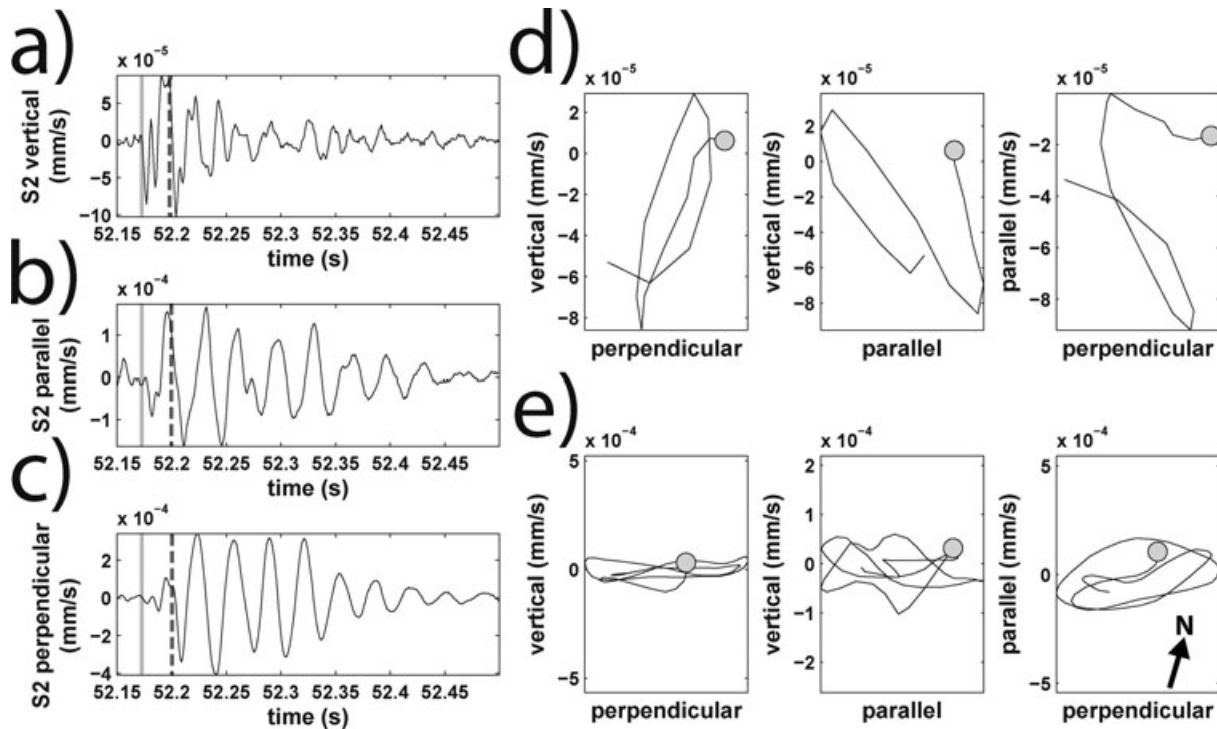


**Figure 6.** Polarization analysis performed on the seismograms recorded at seismometer S2 for the microearthquake of 2007 September 28 at 15.17.39. (a) to (c): Vertical, parallel and perpendicular to the rupture plane signals. *P* and *S* wave arrival times are indicated with a thick grey line and a thick dotted grey line, respectively. (d) and (e) Particle motions in the three polarization planes for *P* waves (duration of 15 ms) and *S* waves (duration of 80 ms), respectively. Motion starts are indicated with grey dots.

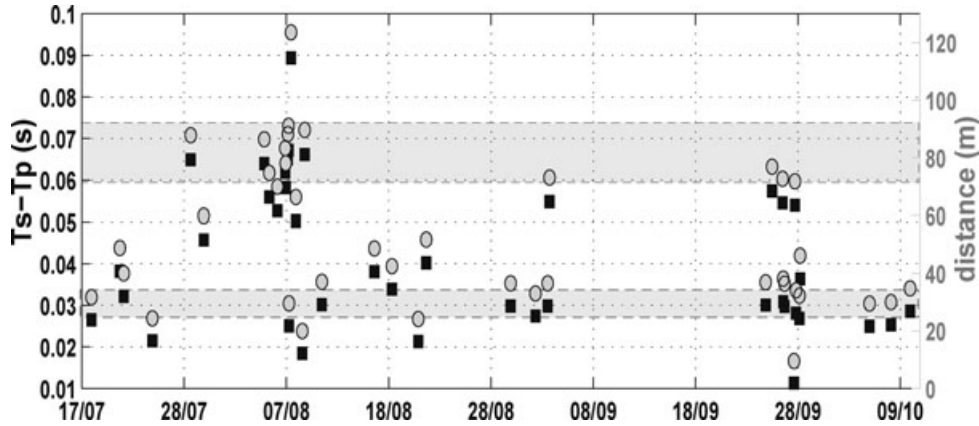


**Figure 7.**  $T_s - T_p$  values (black squares) picked at seismometer S2 as a function of time. Data are converted in hypocentral distances (grey circles) (see text for details). The distance scale is given on the right of the diagram. The two zones exhibiting fresh ruptures are shaded (Section 1).

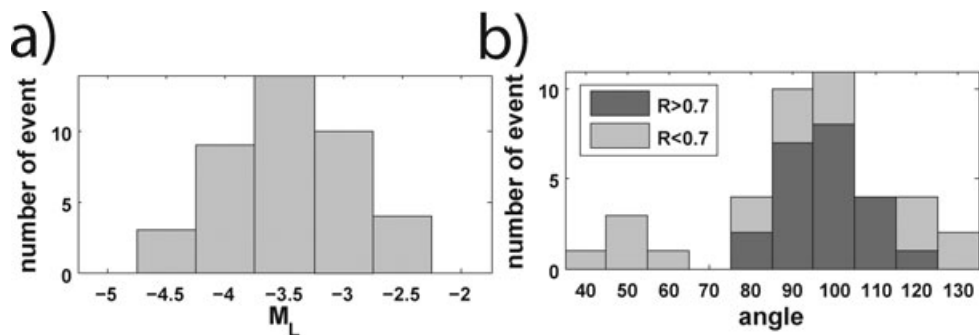


**Figure 8.** (a) Bar diagram of the magnitude distribution. (b) Bar diagram of the polarization angle. Events displaying well defined polarization angle are in dark grey (e.g. correlation coefficient *R* higher than 0.7), whereas the others are in light grey.

seismic events generated during a shaft excavation in granite between 324 and 443 m of depth. They studied the source parameters of 155 tremors with moment magnitude from  $-3.6$  to  $-1.9$ . They found rupture areas between  $0.3$  and  $1.5 \text{ m}^2$  (source radius between  $0.3$  and  $0.7 \text{ m}$ ) which are in a range consistent with the Wells and Coppersmith's relation (rupture area of  $1 \text{ m}^2$  for a magnitude of  $-2$ ).

$S$ -wave polarization diagrams of the 3C sensor S2 were calculated for the 40 events (Fig. 9). The  $S$ -wave polarization in the horizontal plane (Fig. 9a) shows a vibration orientation which is more or less perpendicular to the rupture plane  $\eta$ . A linear regression model was fitted to the  $0.08 \text{ s}$  of signal following the first  $S$ -wave arrival and the correlation coefficient  $R$  was computed. The polarization angle is defined as the angle made by this line and the rupture plane ( $N 165^\circ$ ), and is counted positive for anti-clockwise rotation. The ground motions are considered as linearly polarized when  $R$  is higher than  $0.7$ . The events fitting this criterion are distinguished in Fig. 9(a) ( $R > 0.7$ ). The bar diagram of the polarization angles is drawn in Fig. 8(b). 80 per cent of the values are between  $70^\circ$  and  $110^\circ$ , indicating a preferential orientation perpendicular to the rupture plane. The corresponding motions are predominantly linearly polarized with  $R$  values higher than  $0.7$ . No evolution of the  $S$ -wave polarization angle was observed with time or with hypocentral distance. Polarization diagrams in the vertical plane perpendicular to the rupture plane usually shows predominant horizontal  $S$ -wave motions much higher than vertical  $P$ -wave motions. The link between the polarization diagrams and the rupture mechanism will be numerically studied in Section 6.

## 6 RUPTURE MECHANISM MODELLING

Two main rupture mechanisms could explain the opening of the rear fracture and the collapse of the Chamousset column: slide along a plane with a shear mechanism similar to a normal fault, or topple with a tensile fracture mode. In order to understand the observed polarization patterns for  $P$  and  $S$  waves and to constrain the microearthquake source mechanism, we numerically simulated the ground motions generated by the two possible rupture modes (traction and shear). We applied a code coupling the discrete wave number method (Bouchon 1981; Cotton & Coutant 1997) for computing Green's functions in an axisymmetric medium and the reflectivity method (Kennett & Kerry 1979) for propagating the wavefield in a layered medium. Synthetic seismograms are calculated by convolving Green's functions with a source function.

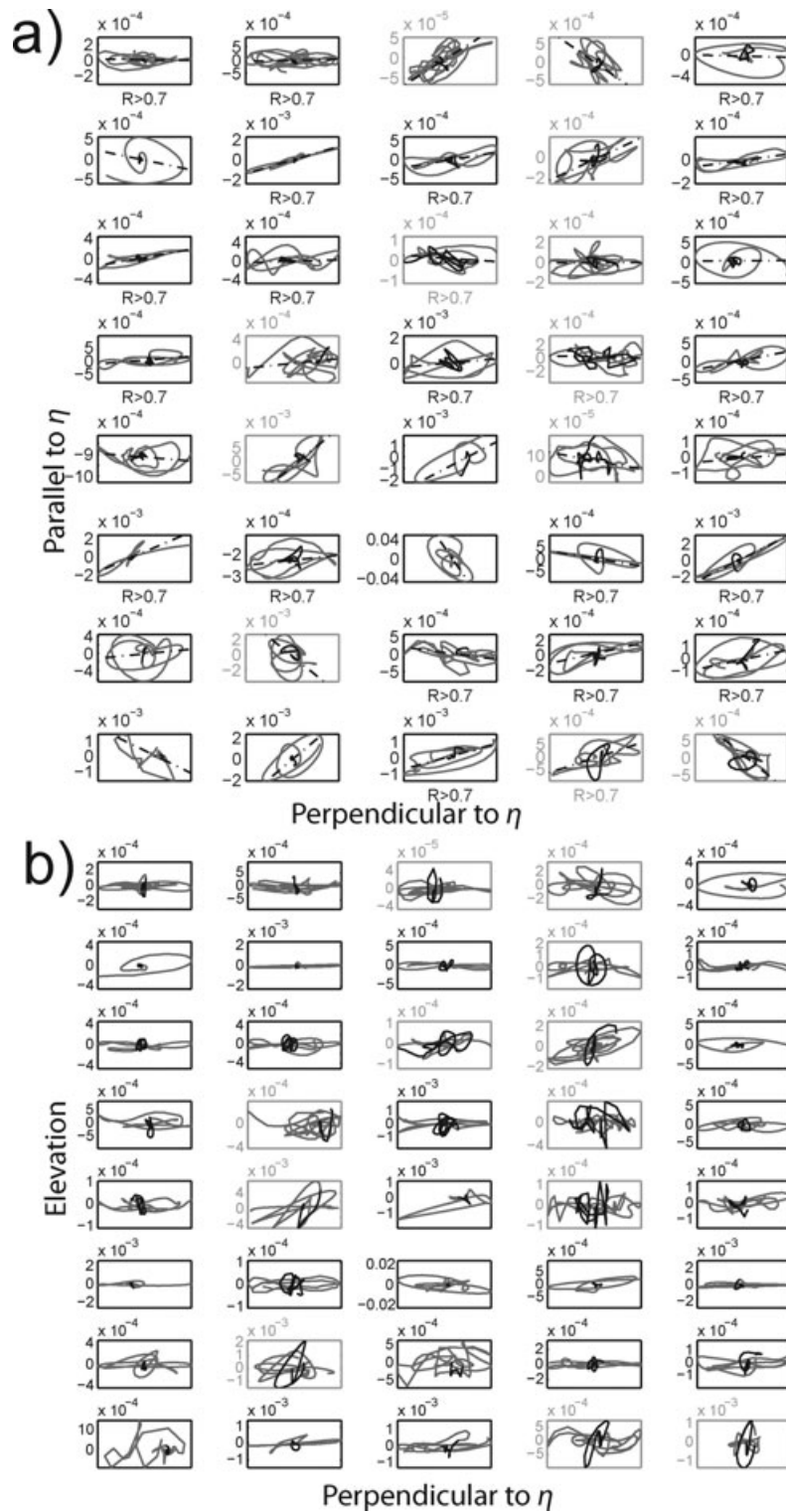
Four simulations were performed with a nine sensor array located at the free surface and a source (in traction or in shear) situated at  $-30$  or  $-75 \text{ m}$  in depth (Fig. 10a). The geometry of the rupture surface was simplified as a plane dipping at  $80^\circ$  (Fig. 10b). The source positions in depth mimic the location of rock bridges observed along the rupture plane (Fig. 2). The source time function is a  $0.03 \text{ s}$  Ricker wavelet for all the simulations and the focal mechanism is either a traction (strike =  $0^\circ$ , dip =  $80^\circ$ ) or a shear (strike =  $0^\circ$ , dip =  $80^\circ$ , rake =  $-90^\circ$ ), in agreement with the convention given in Aki & Richards (2002). The elastic seismic model obtained from refraction tests was used for the simulations, and quality factors values were chosen for this type of material (see Table 2). The 1st two metres thick layer corresponds to soft soil, whereas the 2nd layer corresponds to the calcareous bedrock.

Fig. 11 shows the four sets of polarization diagrams for the two rupture mechanisms and the two source depths. As the problem is symmetrical, the motions at only six sensors (1–6) are shown in the

horizontal plane and in the two vertical planes on both sides perpendicular to the rupture plane. For the shear mode (normal fault mechanism; Figs 11a and c),  $S$ -waves above the source are mainly horizontal and are predominant with regards to  $P$  waves. They are polarized perpendicular to the rupture plane trace, particularly for the source at  $-75 \text{ m}$ . This polarization pattern is very similar to 70 per cent of the observed polarization diagrams (Fig. 9). The observed dispersion in polarization angle (Fig. 8b) probably partly results from the roughness of the rupture surface, which locally exhibits strike and dip variations and, also, from the relative source location compared to the sensor position. For the traction mode (toppling mechanism), the polarization diagrams (Figs 11b and d) also show  $S$ -waves polarized approximately perpendicular to the rupture plane trace, with a more complex shape in the vertical plane. A distinctive feature is that  $P$ -wave vibrations (vertical component) are much higher than those computed for the shear mode, with amplitudes similar to  $S$ -waves. In Fig. 12(a) are plotted the ratios of the maximum amplitudes of  $S$  and  $P$  waves ( $A_s/A_p$ ) in the vertical plane perpendicular to the rupture plane  $\eta$ , as a function of the sensor number for the two rupture mechanisms. Two distinct clusters clearly appear, separated by a ratio threshold of about 3. Fig. 12(b) presents the experimental  $A_s/A_p$  ratios versus the polarization angle. Experimental ratio values are in a range similar to the theoretical ones (from about 1 to 60). Considering a threshold of 3 defines two ensembles of events which could correspond to the two distinct rupture mechanisms. About 30 per cent of the microearthquakes are characterized by  $A_s/A_p$  ratios lower than 3, with poorly defined polarization angles (white triangles). On the contrary, the ground motions of events with high  $A_s/A_p$  ratios are in majority linearly polarized (black circles). These results suggest that the two rupture mechanisms could be distinguished. Fig. 13(a) displays the magnitude of the 40 microearthquakes as a function of the hypocentral distance, distinguishing the two focal mechanisms. Whereas no relation appears between magnitude and hypocentral distance, the majority of the events with a traction mechanism turned out to be located between 20 and 39 m, in the vicinity of the upper zone where rock bridges were observed. On the contrary, most of the shear-like events are scattered between 30 and 90 m. These results suggest that, during the 4-month experiment, toppling seemed to occur predominantly in the upper part of the column. Sliding, which was spread along the column height, was the main rupture mode in the lower part. These results have been obtained for a limited number of microearthquakes and could be biased. The drawn conclusions have to be corroborated by further studies.

## 7 COLUMN MOTION CHARACTERISTICS

So far, we have investigated the information available in the 3-C seismograms recorded on the rock mass. We now compare the vertical signals measured on the rock mass (sensor S2, Fig. 1b) and on the rock column (sensor S1). Fig. 14 shows the seismograms, the corresponding spectrograms and the spectral ratios for three microearthquake events (M1–M3). A striking feature is that the ground motion on the column is systematically higher than on the rock mass, with an amplitude ratio between 2 (event M1) and 50 (event M3) in the time domain. Spectrograms on the rock mass (S2) evidenced energy in different frequency ranges for the three events (first  $0.5 \text{ s}$ ), probably varying with the source location and characteristics. Notably, the higher magnitude event (Fig. 14c) exhibits



**Figure 9.** Polarization diagrams for the 40 microearthquakes recorded at sensor S2. (a) in the horizontal plane. (b) in the vertical plane perpendicular to the rupture plane. Grey line: *S*-wave motion. Black line: *P*-wave motion. Events interpreted as resulting from shear (traction) mechanism have black (grey) axis. Linear regressions (dotted lines on Fig. (a)) are performed on the *S*-waves to deduce polarization angles. Whenever the correlation coefficient *R* of these linear regressions is higher than 0.7, it is written ‘*R* > 0.7’ at the bottom the corresponding subplot.

lower frequency content ([0 10 Hz]) than those observed for the two other events. Spectrograms measured on the rock column (S2) show significant differences with those computed on the rock mass (S1). Spectrogram ratios evidence spectral amplifications at specific but

different frequencies, whose amplitude increases from event M1 (Fig. 14a) to event M3 (Fig. 14c). For events M2 and M3, the energy in the coda (late part of the signal) concentrates at one given frequency (43 Hz) (see spectrograms S1 and spectrogram ratios).

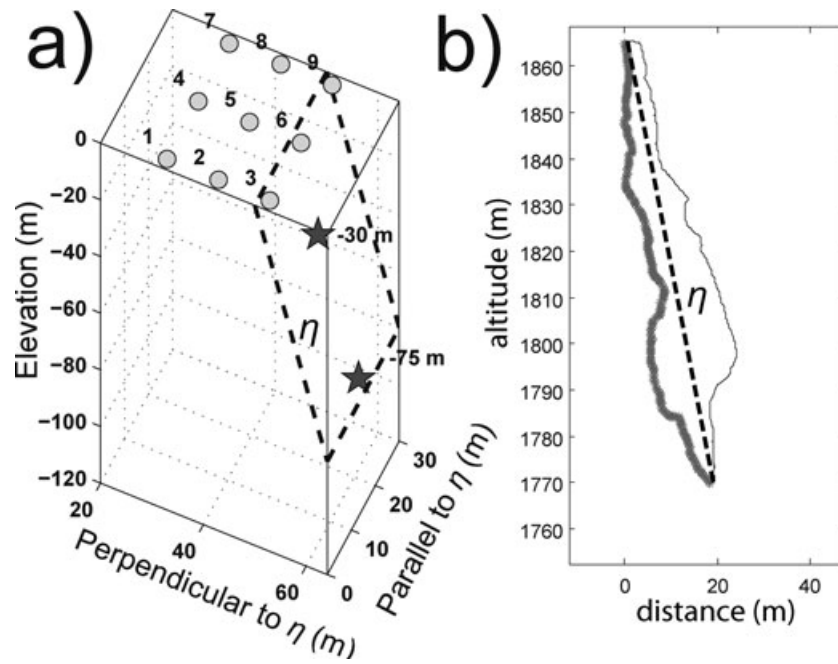


**Figure 10.** Layout of the sensors and sources for the source mechanism simulations. The sensors (labelled from 1 to 9) are represented with grey circles. The rupture plane  $\eta$  ( $80^\circ$  of dip) is marked with black dotted lines. The sources at  $-30$  m and  $-75$  m along the rupture plane are dark stars. The medium is a layered half-space with the characteristics given in Table 2. (b) Vertical cross section through the Chamousset rock column Digital Elevation Model deduced from LIDAR data. The rupture surface is in bold dark line. The mean rupture plane  $\eta$  (dip of  $80^\circ$ ) chosen for the simulation is shown with a black dotted line.

**Table 2.** Dynamic characteristics of the two-layer seismic model used for ground motion simulations.

Layer thickness (m)	<i>P</i> -wave velocity ( $\text{m s}^{-1}$ )	<i>S</i> -wave velocity ( $\text{m s}^{-1}$ )	Density	Quality factor, $Q_p$	Quality factor, $Q_s$
2	430	185	2	40	20
–	2800	960	2.65	1000	500

Two other less energetic lower frequencies also appear at about 3.5 and 6.7 Hz for event M3. These frequencies match some of the column resonance frequency values (3.5, 6.7 and 43 Hz) which were determined from seismic noise analysis (Levy *et al.* 2010).

These observations show that microearthquakes could excite the rock column at some of its resonance frequencies, depending on the spectral characteristics and the location of the source. In Fig. 13(b) are plot the column-to-mass amplitude ratio versus hypocentral distance from sensor S2 for the 40 microearthquakes, distinguishing events with long coda dominated by resonance frequencies. Highest ratios (over 3) are clearly associated with a longer coda, highlighting the role of resonance phenomena in the motion amplification on the column. Also, most of the microearthquakes exhibiting a longer coda seem to be located along or close to the zones with fresh rock ruptures (Fig. 13b).

To understand these observations, the 2-D dynamic response of the rock column to nearby seismic events was numerically modelled for different source locations. Fig. 15(a) presents the geometry of the 2-D model with the Chamousset rock column (Fig. 15b) attached to the mass by rock bridges. The elastic dynamic characteristics of the layers are derived from the seismic prospecting (Table 2). Four sources were introduced in the model: two along the rock mass-column interface at 30 and 75 m depth, and two in the rock mass at the same depths (Fig. 15b). The source mechanism is a simple horizontal point force with a 0.03 s Ricker wavelet as time function.

Synthetic seismograms were computed using the explicit dynamic finite element code Plast2 (Baillet *et al.* 2005; Levy *et al.* 2010), using 9245 quadrilateral finite elements with absorbing boundaries and a minimum element size  $h$  of 0.4 m. Details on the numerical method can be found in Levy *et al.* (2010).

Simulation results for sources R1 and R2 are shown in Fig. 16 with the same presentation as in Fig. 14. For the source located in the rock mass (position R1, Fig. 15b), the motion amplitude and the frequency content (between 20 and 50 Hz) of signal S2 measured on the mass are similar for the two components (Figs 16a and b). On the contrary, the motion spectral characteristics on the rock column (S1) differ between the horizontal and vertical components, with a concentration of energy at given frequencies (e.g. 35 Hz for the vertical component), associated with a signal amplification of 2–3. The spectrogram at sensor S1, as well as the spectrogram ratio, evidences energy at some specific frequencies in the late coda along the horizontal component (3 and 10 Hz). This phenomenon is less visible along the vertical component. When the seismic source is located along the interface (source R2 located in the upper rock bridge breakage zone; Figs 16c and d), seismograms show a dramatic motion amplification on the column, with an amplitude of 5 and 11, on the vertical and horizontal components, respectively. Analysis of the spectrograms computed on the rock column (S2) and of the spectrogram ratios S1/S2 clearly evidences a concentration of seismic energy at some specific frequencies (3, 10, 20, 29, 35 and 40 Hz), both in the early and late parts of the signals. This phenomenon is particularly apparent along the horizontal component, for which spectral ratios as high as ten were computed. We calculated the five first theoretical resonance frequencies of the column (3.2, 9.8, 12.6, 15.1 and 19.4 Hz) and a very good agreement was found between the frequencies which concentrate energy and the resonance frequency values. Similar numerical results (not shown here) were obtained for sources R3 and R4 located at 75 m depth (Fig. 15b).

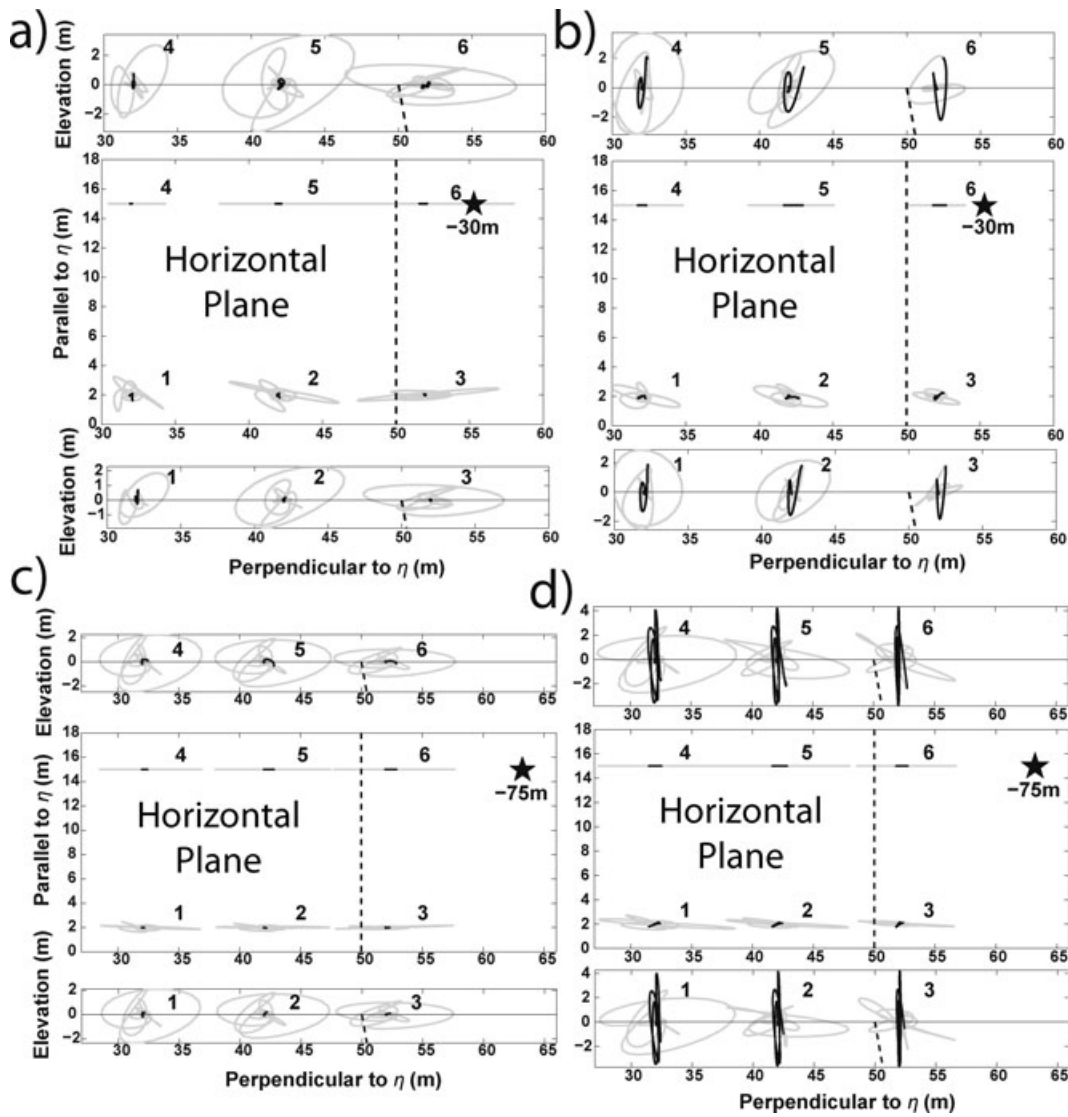


**Figure 11.** Simulated polarization diagrams of  $P$  waves (black lines) and  $S$  waves (grey lines) for sensors 1–6 (Fig. 10). The trace of the rupture plane  $\eta$  is shown with a black dotted line. (a) Source at  $-30$  m with a shear mechanism. (b) Source at  $-30$  m with a traction mechanism. (c) Source at  $-75$  m with a shear mechanism. (d) Source at  $-75$  m with a traction mechanism. For each source are shown the motions in the horizontal plane and in the two vertical planes along the sensor lines.

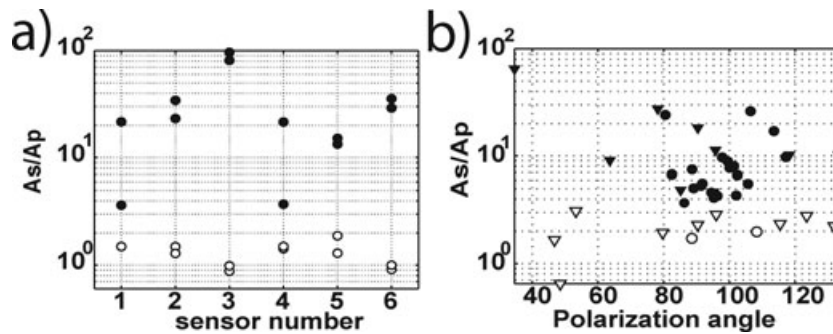


**Figure 12.** (a) Ratios of the maximum amplitudes of  $S$  and  $P$  waves (in the vertical plane perpendicular to the rupture plane  $\eta$ ) as a function of the sensor number for synthetic data. (b) The same as a function of the polarization angle for experimental data. Shear and traction mechanisms are shown with black and white markers, respectively. In (b), events displaying a correlation coefficient  $R < 0.7$  are plotted with triangles.

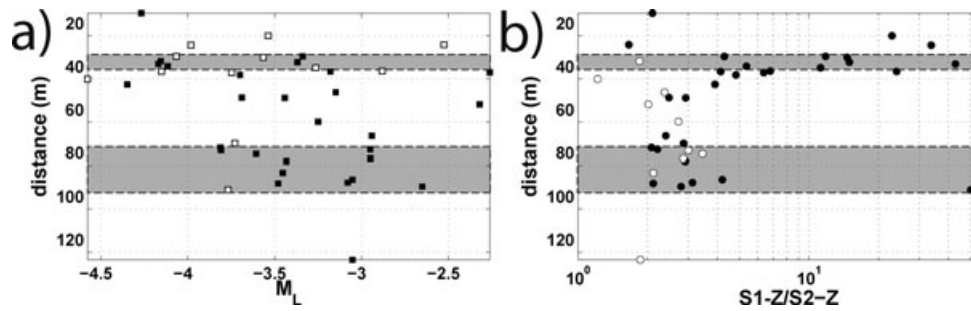


**Figure 13.** (a) Estimated hypocentral distance from sensor S2 versus the magnitude for the 40 microearthquakes. Shear and traction mechanisms are shown with black and white squares, respectively. (b) Estimated hypocentral distance from sensor S2 versus the maximum amplitude ratio between the vertical (z) signals measured on the rock column (S1) and on the rock mass (S2). Microearthquakes displaying a long coda are shown with black circles. The two zones exhibiting fresh ruptures are shaded.

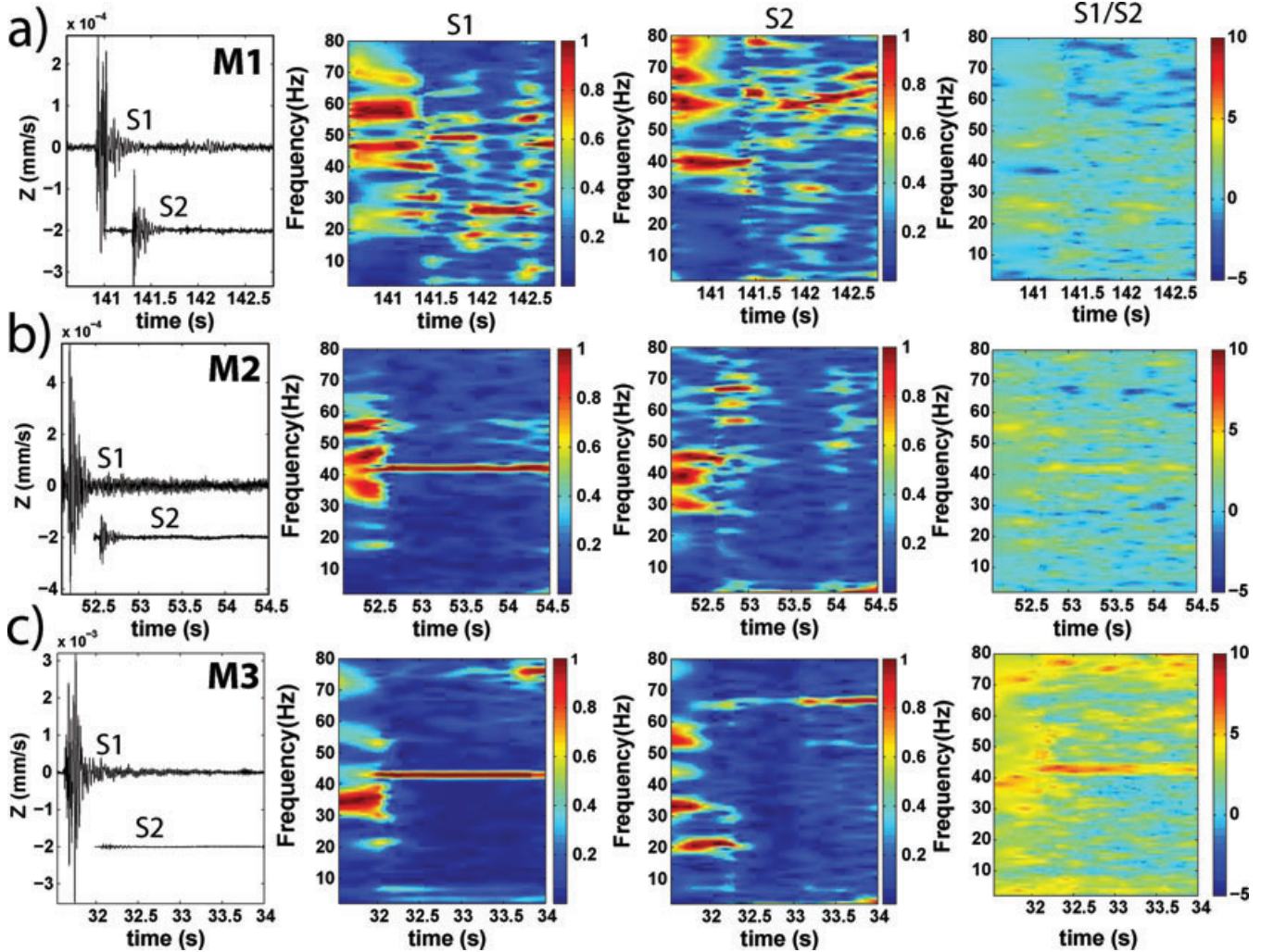


**Figure 14.** Vertical seismograms (1st column), normalized spectrograms (2nd and 3rd columns) and spectrogram ratio in log scale (4th column) for three microearthquakes (M1–M3). Seismograms were recorded on the rock column (sensor S1) and on the rock mass (sensor S2). Seismograms of sensor S2 (of lower amplitude) are shifted by 0.5 s and by two unities along the X and Y axis, respectively. Spectrograms (S2 and S1) are computed with a window length of 0.8 s and 98 per cent of overlap. (a) Microearthquake ( $M_L = -4.15$ ) showing no coda pattern, recorded the 2007 July 18 at 22:50:23. (b) Microearthquake ( $M_L = -4.11$ ) showing a mono-frequency coda at 43 Hz, recorded the 2007 September 28 at 15:17:39. (c) Microearthquake ( $M_L = -3.76$ ) showing a coda with energy at peak frequencies (3.5, 6.7 and 43 Hz), recorded the 2007 August 8 at 00:03:31.

In summary, numerical simulations mimic the stronger ground motions observed on the rock column with regards to the rock mass, as well as the energy concentration at specific resonance frequencies. This suggests that the motion amplification results from the

column resonance triggered by the seismic events. Modelling also evidenced the predominant effect of the source location on the dynamic response of the column. Higher amplifications and longer coda were simulated for sources acting along the column-to-mass

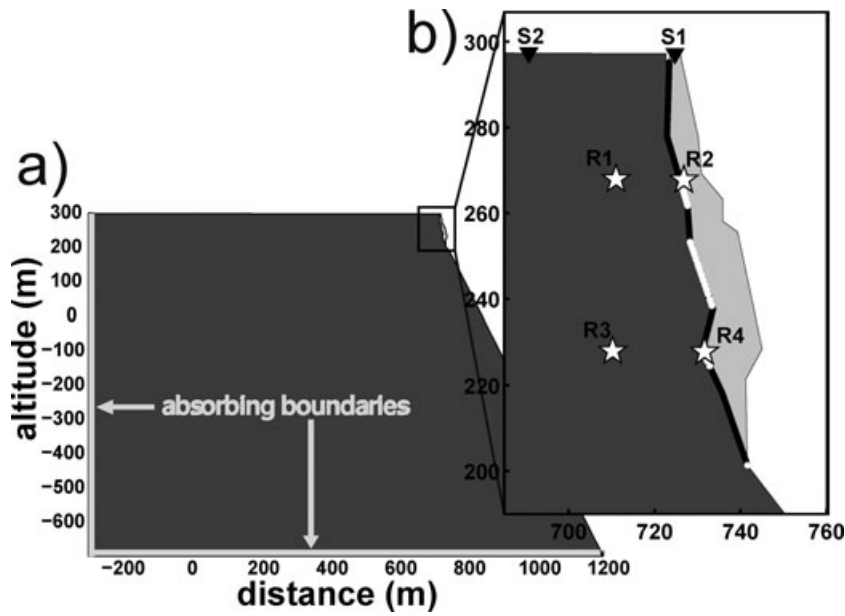


**Figure 15.** Geometry of the rock mass and of the column, both including a 2 m thick low velocity layer at the top. (b) Cross-section through the Chamousset column with the location of two seismic sensors (black triangles) and of the different sources (with stars labelled R1–R4). White dots along the interface indicate the zones with rock bridges or with a friction contact. Black dots denote no contact.

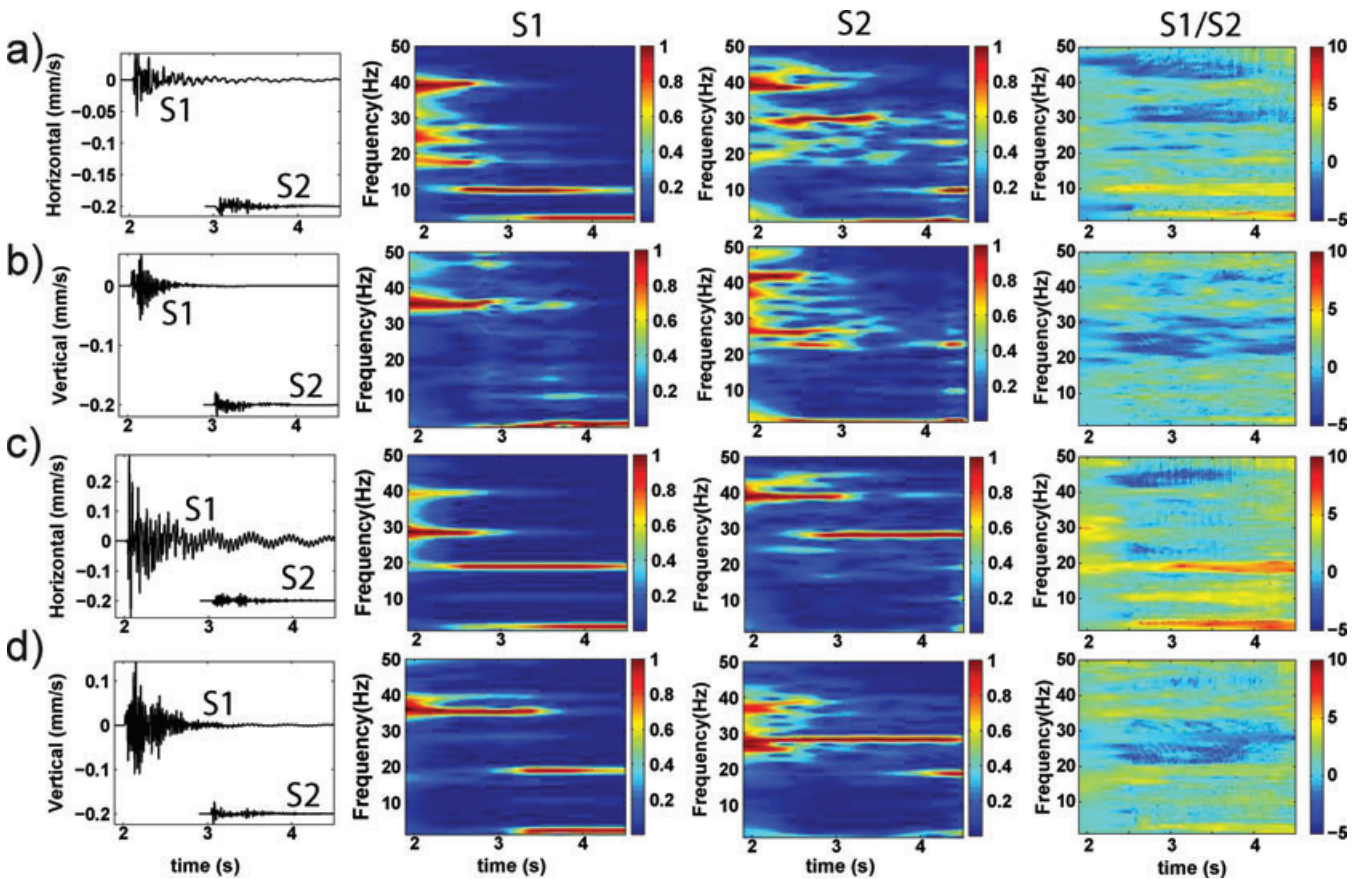


**Figure 16.** First column: Synthetic seismograms at sensors 1 and 2 (shifted). 2nd to 3rd column: spectrograms at sensors 1 and 2, respectively. 4th column: spectrogram ratio of sensors 1 over 2 with a log scale. (a) and (b) Source R1: motions along the horizontal and vertical components, respectively. (c) and (d) Source R2: motions along the horizontal and vertical components, respectively.

interface. This association of high motion amplification ( $>3$ ) and longer duration was also observed in the measurements and could serve as a criterion for identifying events related to rock bridge breakage along the interface. Although a general good agreement was found between the simulated and measured seismic motion characteristics (including resonance frequencies), some discrepancies exist on the more excited resonance frequencies. In particular, numerical modelling failed to simulate the observed predominance of the 43 Hz frequency in the coda on the rock column (compare Figs 14a and 16d for sensor S1), as well as the highest amplifications (over 12). This discrepancy could result from the 2-D modelling approximation and from a difference in the source spectral signature and mechanism, which strongly control the column excitation. Also, the attenuation properties of the medium (which are unknown here) could play a significant role in resonance phenomena and could modify the energy amplification and repartition between the natural frequencies.

## 8 CONCLUSIONS

A small-aperture short-period seismic array monitored the seismic activity during a 4-month period preceding a column fall (21 000 m<sup>3</sup>) in the Vercors massif (Western French Alps). Almost 200 events were recorded by the seven seismometers of the 40 m aperture array. Apart of distant events (earthquakes and quarry blasts), signal analysis has evidenced three main types of nearby seismic events (microearthquakes, individual block falls and rock falls) which showed distinctive temporal and spectral characteristics. Microearthquakes (single or multiple events) are the more numerous (62 per cent of the events), followed by rock falls (12 per cent), earthquake type events (5 per cent) and block falls (4 per cent). Finally, 17 per cent of the events were unclassified and probably correspond to a complex mixing of nearby rupture events and rock or block falls with very short delays, which made impossible any clear identification. A relation was found between the daily number of seismic events and the temperature values. The largest numbers of events fit with minima in the temperature curve, after a severe temperature drop (from 15 to 20°C). This result suggests a temperature control on rupture events and damaging, as it was recently shown from resonance frequency analysis on the same site (Levy *et al.* 2010).

The polarization analysis of 40 microearthquake seismograms with a good signal-to-noise ratio allowed *P* and *S* waves to be identified on the only 3-C sensor of the array. The magnitude of these microearthquakes ranges from  $-4.5$  and  $-2$ . Using a simple seismic model derived from refraction tests performed on the plateau, we transformed *Ts-Tp* values in hypocentral distances from the sensor. Most microearthquakes are located in a distance range compatible with the two zones exhibiting fresh rupture along the scarp. No accurate location was possible using the six vertical sensors and the one 3-C sensor, probably because of the complex velocity structure at the site. The polarization patterns were numerically modelled for the two possible rupture mechanisms (sliding with a shear mode and toppling with a traction mode). Comparison between observed and simulated polarization diagrams showed that 30 per cent of the microearthquakes were probably generated by traction in the upper part of the column, while the remaining 70 per cent were shear-rupture events, distributed in the two rupture zones. These results indicate that the two rupture modes coexisted in different zones before the fall. Comparison of the vertical ground motions on the prone-to-fall column and on the rock mass showed a higher amplitude on the column. In particular, 60 per cent of

the 40 microearthquakes generated an amplification higher than 3, associated with a longer coda dominated by specific frequencies. These events turned out to be located at hypocentral distances from the 3-C sensor, which are in a range compatible with the fresh rupture zones observed after the collapse. 2-D numerical modelling of the dynamic response of the column to nearby seismic events successfully simulated the motion amplification observed on the rock column. Higher amplification values and longer coda with dominant frequencies were retrieved when sources were located along the column-to-mass interface. Dominant frequencies were found to be natural column frequencies. All these results suggest that seismic events generating high motion amplification ( $>3$ ) and longer coda duration result from rock bridge breakage along the interface. This study has shown that the analysis of the signals generated before a rock failure could bring some insight on the rupture mechanisms, at least in a stiff rock like limestone.

## ACKNOWLEDGMENTS

Many thanks to O. Coutant for his helpful comments on running the code AXITRA. This work was partially funded by the A.N.R Triggerland, the federative structure V.O.R (Vulnérabilité des Ouvrages aux Risques), the Alcotra project MASSA and the Marie Curie Program 'Mountain Risks'. This work would not have been achieved without the help of many field work participants; we are especially grateful to R. Béthoux and G. Cougoulat, as well as to the rangers of the Vercors Regional Park for drawing our attention to the Chamouset site and for allowing the deployment of a scientific experiment in a protected area. Most of the computations were performed at the 'Service Commun de Calcul Intensif de l'Observatoire de Grenoble (SCCI)'. The authors are also grateful to the 'parc national Sismob (INSU-CNRS)' and to the LGIT for lending the seismic instruments.

## REFERENCES

- Aki, K. & Richards, P., 2002. *Quantitative Seismology*, Univ. Science Books, Mill Valley, CA.
- Amitrano, D., Grasso, J.R. & Senfaute, G., 2005. Seismic precursory patterns before a cliff collapse and critical point phenomena, *Geophys. Res. Lett.*, **32**(8), L08314.
- Amitrano, D., Arattano, M., Chiarle, M., Mortara, G., Occhiena, C., Pirulli, M. & Scavia, C., 2010. Microseismic activity analysis for the study of the rupture mechanisms in unstable rock masses, *Nat. Hazards Earth Syst. Sci.*, **10**(4), 831–841.
- Baillet, L., Linck, V., D'errico, S., Laulagnet, B. & Berthier, Y., 2005. Finite element simulation of dynamic instabilities in frictional sliding contact, *J. Tribol.*, **127**(3), 652–657.
- Bouchon, M., 1981. A simple method to calculate Green's functions for elastic layered media, *Bull. seism. Soc. Am.*, **71**(4), 959–971.
- Burjánek, J., Gassner-Stamm, G., Poggi, V., Moore, J.R. & Fäh, D., 2010. Ambient vibration analysis of an unstable mountain slope, *Geophys. J. Int.*, **180**(2), 820–828(9).
- Cotton, F. & Coutant, O., 1997. Dynamic stress variations due to shear faults in a plane-layered medium, *Geophys. J. Int.*, **128**(3), 676–688.
- Cruden, D. & Varnes, D., 1996. Landslide investigation and mitigation, Transportation Research Board Special Report, *Landslide Types and Processes*, pp. 36–71, National Academy of Sciences, Washington DC.
- Del Gaudio, V. & Wasowski, J., 2007. Directivity of slope dynamic response to seismic shaking, *Geophys. Res. Lett.*, **34**(12), L12301.
- Del Gaudio, V., Coccia, S., Wasowski, J., Gallipoli, M.R. & Mucciarelli, M., 2008. Detection of directivity in seismic site response from microtremor spectral analysis, *Nat. Hazards Earth Syst. Sci.*, **8**(4), 751–762.

- Deparis, J., Jongmans, D., Cotton, F., Baillet, L., Thouvenot, F. & Hantz, D., 2008. Analysis of rock-fall and rock-fall avalanche seismograms in the French Alps, *Bull. seism. Soc. Am.*, **98**(4), 1781–1796.
- Frayssines, M. & Hantz, D., 2006. Failure mechanisms and triggering factors in calcareous cliffs of the subalpine ranges (French Alps), *Eng. Geol.*, **86**(4), 256–270.
- Gibowicz, S.J., Young, R.P., Talebi, S. & Rawlence, D.J., 1991. Source parameters of seismic events at the underground research laboratory in Manitoba, Canada: Scaling relations for events with moment magnitude smaller than -2, *Bull. seism. Soc. Am.*, **81**(4), 1157–1182.
- Got, J.-L., Mouroit, P. & Grangeon, J., 2010. Pre-failure behaviour of an unstable limestone cliff from displacement and seismic data, *Nat. Hazards Earth Syst. Sci.*, **10**(4), 819–829.
- Heincke, B., Maurer, H., Green, A.G., Willenberg, H., Spillmann, T. & Burlini, L., 2006. Characterizing an unstable mountain slope using shallow 2D and 3D seismic tomography, *Geophysics*, **71**(6), B241–B256.
- Helmstetter, A. & Garambois, S., 2010. Seismic monitoring of S echilienne rockslide (French Alps): Analysis of seismic signals and their correlation with rainfalls, *J. geophys. Res.*, **115**(F3), F03016.
- Joswig, M., 2008. Nanoseismic monitoring fills the gap between microseismic networks and passive seismic, *First Break*, **26**(6), 121–128.
- Kennett, B.L. & Kerry, N.J., 1979. Seismic waves in a stratified half space, *Geophys. J.R. astr. Soc.*, **57**, 557–583.
- Lacroix, P. & Helmstetter, A., 2010. Location of seismic signals associated with micro-earthquakes and rockfalls on the S echilienne landslide, French Alps, *Bull. seism. Soc. Am.*, in press.
- Levy, C., Baillet, L., Jongmans, D., Mouroit, P. & Hantz, D., 2010. The dynamic response of the chamousset rock column (Western Alps, France) before its collapse, *J. geophys. Res.*, **115**, F04043.
- Mertl, S. & Br uckl, E., 2007. Observation of fracture processes in creeping rock masses by seismic monitoring, in *Proceedings at 11th Congress of the International Society for Rock Mechanics*, Lisbon, Portugal.
- Renalier, F., Bi evre, G., Jongmans, D., Campillo, M. & Bard, P.-Y., 2010. *Characterization and Monitoring of Unstable Clay Slopes Using Active and Passive Shear Wave Velocity Measurements*, Geophysical Developments Series no. 15, ch. 24, pp. 397–414, SEG.
- Senfaute, G., Duperret, A. & Lawrence, J.A., 2009. Micro-seismic precursory cracks prior to rock-fall on coastal chalk cliffs: a case study at Mesnil-Val, Normandie, NW France, *Nat. Hazards Earth Syst. Sci.*, **9**(5), 1625–1641.
- Spillmann, T., Maurer, H., Green, A.G., Heincke, B., Willenberg, H. & Husen, S., 2007. Microseismic investigation of an unstable mountain slope in the Swiss Alps, *J. geophys. Res.*, **112**, B07301.
- Thouvenot, F., Fr echet, J., Guyoton, F., Guiguet, R. & Jenatton, L., 1990. Sismalp: an automatic phone-interrogated seismic network for the Western Alps, *Cahiers du Centre Europ een de G eodynamique et de S eismologie*, **1**, 1–10.
- Vilajosana, I., Suri nach, E., Abell an, A., Khazaradze, G., Garcia, D. & Llosa, J., 2008. Rockfall induced seismic signals: case study in Montserrat, Catalonia, *Nat. Hazards Earth Syst. Sci.*, **8**(4), 805–812.
- Walter, M. & Joswig, M., 2008. Seismic monitoring of fracture processes generated by a creeping landslide in the Vorarlberg Alps, *First Break*, **26**(6), 131–135.
- Walter, M. & Joswig, M., 2009. Seismic characterization of slope dynamics caused by softrock-landslides: the Super-Sauze case study, in *Landslide Processes: from Geomorphological mapping to dynamic modelling*, pp. 215–220, CERG Editions, Strasbourg.
- Wells, D.L. & Coppersmith, K.J., 1994. New empirical relationships among magnitude, rupture length, rupture width, rupture area, and surface displacement, *Bull. seism. Soc. Am.*, **84**(4), 974–1002.